Ni-Fe (oxy)hydroxide Modified Graphene Additive Manufactured (3D-Printed) Electrochemical Platforms as an Efficient Electrocatalyst for the Oxygen Evolution Reaction

Dr Pãmyla L. dos Santos[1,2,3], Dr Samuel J. Rowley-Neale,[2,3] Dr Alejandro G-M. Ferrari,[2,3] Dr Juliano A. Bonacin,[1] and Prof Craig E. Banks[2,3*]*

[1]: Institute of Chemistry, University of Campinas, P. O. Box 6154, 13083-970, Campinas, SP, Brazil.

[2]: Faculty of Science and Engineering, School of Science and the Environment, Division of Chemistry and Environmental Science, Manchester Metropolitan University, Chester Street, Manchester M1 5GD, UK.

[3]: Manchester Fuel Cell Innovation Centre, Manchester Metropolitan University, Chester Street, Manchester M1 5GD, UK.

*To whom correspondence should be addressed.

Email: c.banks@mmu.ac.uk; Tel: ++(0)1612471196; Fax: ++(0)1612476831.

jbonacin@unicamp.br; Tel: +55(19)35213103; Fax: +55(19)35213023;

Website: www.craigbanksresearch.com; www.bonacin.iqm.unicamp.br

1. Abstract

We demonstrate that polylactic acid (PLA)/graphene additive manufactured (3D-printed) electrodes (Gr/AMEs) electrodeposited with Ni-Fe (oxy)hydroxide can efficiently catalyse the oxygen evolution reaction (OER). X-ray photoelectron spectroscopy (XPS) depth profiling combined with Atomic Force Microscopy (AFM) and Tip Enhanced Raman Spectroscopy (TERS) deduced the composition and depth of the Ni-Fe (oxy)hydroxide layer. The composition of the resulting electrocatalytic surface are be tailored through altering the concentrations of nickel and iron within the electrodeposited solutions, which give rise to optimised AMEs OER performance (within 0.1 M KOH).

The optimal OER performance was observed using Ni-Fe (oxy)hydroxide with a 10% content of Fe, displaying an OER onset potential and overpotential of + 1.47 V (*vs*. RHE) and 519 mV, respectively, which is comparable to that of polycrystalline Iridium (+ 1.43 V (*vs*. RHE) and *ca.* 413 mV), as well as being significantly less electropositive than a bare/unmodified AME. This work is essential for those designing, fabricating and modulating additive manufactured electrodes.

2. Introduction

As the global energy demand is set to increase by 30% from 2016 to 2040,[1] there is a strong impetus to employ non-polluting energy generation techniques to meet this increased demand, as fossil fuel (FF) alternatives are likely to exasperate the effects of anthropogenic climate change. The major limiting factor to the ubiquitous implementation of renewable energy sources within a power grid is there often poor correlation to consumer demand. Methods of storing the generated energy for use, as and when required are therefore vital. A promising potential approach is hydrogen gas generated *via* water splitting within a water electrolyser, which can be produced upon demand,[2] and for example be utilized within a hydrogen fuel cell to produce power for a plethora of applications.

Water electrolysis consists of two half-cell reactions. Those being the production of oxygen on the anode *via* oxygen evolution reaction (OER),[3] and the production of hydrogen on the cathode *via* hydrogen evolution reaction (HER).[4],[5] The reaction mechanisms for these reactions are dependent upon whether they occur within an acidic or alkaline environment, as described below:

Overall reaction:

$$2H_2O \rightarrow O_2 + 2H_2 \qquad (1)$$

Acid media, pH 0:

$$4H^+ + 4e^- \rightarrow 2H_2 \qquad E_{cathode} = 0\ V \qquad (2)$$

$$2H_2O \rightarrow O_2 + 4H^+ + 4e^- \qquad E_{anode} = 1.23\ V \qquad (3)$$

Alkaline media, pH 14:

$$4H_2O + 4e^- \rightarrow 2H_2 + 4OH^- \qquad E_{cathode} = -0.83\ V \qquad (4)$$

$$4OH^- \rightarrow O_2 + 2H_2O + 4e^- \qquad E_{anode} = -0.40\ V \qquad (5)$$

The practical application of water splitting is limited due to the sluggish kinetics of the OER, which typically requires a noble metal-based catalysts, such as ruthenium and iridium oxides,[6] to occur

efficiently. However, RuO_2 and IrO_2 are unstable in anodic conditions due to the formation of soluble species with high oxidation states, such as RuO_4 and IrO_3/IrO_4^{2-}, respectively.[7] Additionally, their high-cost and low earth abundances limits their attractiveness. Research have therefore focused upon the development of new catalysts that are electrocatalytically competitive with Ir and Ru oxides, whilst being more earth abundant, stable in strong oxidizing conditions and comparatively cheap.[8]

The first-row transition metals (oxy)hydroxides, are promising alternatives to noble metal-based electrocatalysts with numerous studies exploring their OER activity (see Table 1). For example Jaśkaniec *et al.*[9] reported the ability of Ni-Fe layered double hydroxide (LDH) platelets to electrochemically reduce the OER overpotential (recorded at 10 mA cm^{-2}) of nickel foam electrodes from 430 mV to 360 mV. The electrocatalytic activity displayed by Ni-Fe based catalyst is due to the OER mechanism involving the formation of MOH, MO and MOOH intermediates.[10] In alkaline conditions, O_2 can be produced *via* a direct reaction between MO intermediates (Equations 6-8), or *via* the formation of MOOH species (Equations 9-12).[11] This results in an OER catalysts catalytic activity being dependent upon on the interactions (adsorption and desorption), between the metallic reactive sites and the intermediates.[4] Thus, the superior activity of NiOOH when compared to Co, Fe and Mn (oxy)hydroxide family, has been ascribed to the optimal bonding strength of Ni-O.[12] Furthermore, the catalytic activity of NiOOH can be enhanced by incorporating Fe on a percentage mass ratio. The exact role of Fe on the performance of $Ni_{1-x}Fe_xOOH$ catalysts to date remains unclear, however there are numerous and theoretical/computational studies,[13] and in-operando experiments that postulate Fe's role in electrocatalyst.[14]

Direct combination of 2MO intermediates:

$$2M + 2OH^- \rightarrow 2MOH + 2e^- \quad (6)$$

$$2MOH + 2OH^- \rightarrow 2MO + 2H_2O_{(l)} + 2e^- \quad (7)$$

$$2MO \rightarrow 2M + O_{2(g)} \quad (8)$$

Formation of MOOH intermediates:

$$M + OH^- \rightarrow MOH + e^- \quad (9)$$

$$MOH + OH^- \rightarrow MO + H_2O_{(l)} + e^- \quad (10)$$

$$MO + OH^- \rightarrow MOOH + e^- \quad (11)$$

$$MOOH + OH^- \rightarrow M + O_{2(g)} + H_2O_{(l)} + e^- \quad (12)$$

As can be seen in Table 1, several substrates, such as nickel foam,[9, 15] gold,[14a] and glassy carbon,[16] electrodes, have been used for deposition of $Ni_{1-x}Fe_xOOH$. Recently, Xiang *et al*.[17] reported the use of Fe-Ni alloy foil as a substrate to grow vertically aligned Ni-Fe (oxy)hydroxide, which allows a facile access to the catalytic sites and a favourable adsorption of OH intermediate during OER. However, these electrodes lack transferability to "real world"/industrial applications. Utilising additive manufacturing (3D-printing), particularly fused filament fabrication (FFF), to produce electrodes offers several advantages over traditional electrodes, such as the electrodes can be produced quickly, cheaply and in geometries not possible by any other technique.[11] Previous studies have utilised additive manufacturing to develop supercapacitors,[18] batteries,[19] and electrochemical sensors.[20]

Herein, we report for the first time, the use of cost-effective Ni-Fe (oxy)hydroxides modified graphene additive manufactured (3D-printed) electrodes (Gr/AMEs) as highly efficient electrocatalysts for the OER in alkaline medium. The AMEs were electrochemically pre-treated to form films of Ni or Ni-Fe (oxy)hydroxide with a variable Fe content (5, 10, 20 and 40%).

3. Experimental Section

3.1 Chemicals

Potassium chloride (KCl), Potassium hydroxide (KOH), potassium hexacyanidoferrate(II) ($K_4[Fe(CN)_6]$), hexaammineruthenium(III) chloride ($[Ru(NH_3)_6]Cl_3$), potassium hexachloroiridate(III) ($K_3[IrCl_6]$) were purchased from Sigma-Aldrich. Conductive Graphene 3D Printing PLA Filament was purchased from Black Magic 3D.27 (volume resistivity: 0.6 Ω cm^{-1}). All chemicals were of analytical grade and used without any further purification. The aqueous solutions were prepared with ultrapure water (>18 MΩ cm^{-1}) obtained from a Milli-Q Plus system (Millipore).

3.2. Design and fabrication of the electrodes

The graphene additive manufactured/3D-printed electrodes (Gr/AMEs) were produced from commercial conductive graphene/polylactic acid filament "Black magic". The electrodes were drawn using TinkerCAD™, a free online 3D CAD design tool, in the forms of discs with diameters of 5 mm and thicknesses of 1 mm. A strip with a 2 mm thickness was drawn to allow the connection of the electrode to a crocodile clip. The electrodes were printed with a resolution of 0.2 mm per layer, using a RepRap Graber i3 printer with nozzle temperature of 190°C and bed temperature of 90 ºC.

3.3. Electrode modification

Before the electrodeposition of the $Ni(OH)_2$ or $Ni_{1-x}Fe_xOOH$, the Gr/AMEs were submitted to an electrochemical pre-treatment in 0.1 M PB solution (pH 7.4). Then, films of $Ni(OH)_2$ were produced from 10 M $NiSO_4{\cdot}6H_2O$. Bimetallic hydroxide films were obtained from varied concentrations of $NiSO_4{\cdot}6H_2O$ and $FeSO_4{\cdot}7H_2O$ with total metal content of 10 M. Electrodeposition was carried out by chronopotentiometry as reported by Louie *et al.*[14a] applying a cathodic current density of 50 µA cm^{-2} for 1125 s. Figure 1 shows an illustration of the pre-treatment of the graphene 3D-printed electrodes and the electrodeposition of the Ni or Ni-Fe (oxy)hydroxides catalysts. The electrochemical curves

resulted from these processes, chronocoulometric, cyclic voltammogram and choronoamperometric curves are presented in Figure 1.

3.4. Electrochemical measurements

Cyclic voltammetry (CV) and linear sweep voltammetry (LSV) measurements were carried out using an AUTOLAB PGSTAT101 driven by NOVA 2.0 software. The pre-treated bare/unmodified or modified graphene 3D-printed electrode was used as working electrode, saturated calomel electrode (SCE) as a reference electrode, note that the obtained potential values have been converted to a reversible hydrogen electrode ($E_{RHE} = E_{SCE} + 0.059pH + 0.242$) for comparative purposes, and a platinum wire as counter electrode. Oxygen was removed by bubbling nitrogen for 15 min through the solution before each electrochemical measurement.

To study oxygen evolution reaction (OER), linear sweep voltammetry (LSV) measurements were performed in 0.1 M KOH at a scan rate of 10 mV s^{-1}. The stability of the modified additive manufactured (3D printed) electrode was evaluated by applying 1000 voltammetric cycles in 0.1 M KOH at 100 mV s^{-1}. For stability study, a carbon screen-printed electrode was used as counter electrode in order to prevent migration of Pt to the working electrode.

3.5. Characterization

The morphologies of the bare and modified AMEs were analyzed by scanning electron microscope (SEM) using a Zeiss SUPRA 40 (Carl Zeiss Ltd, Germany). Composition of the electrodes were investigated by energy dispersive X-rays spectroscopy (EDS) using an Apollo 40 SDD (EDAX Inc., USA), coupled to the SEM. Raman spectra were recorded using a Renishaw inVia Raman microscope spectrometer (Renishaw PLC, UK) equipped with an argon laser (λ = 514.3 nm). X-ray photoelectron spectra (XPS) XPS depth profiling and measurements were obtained using a Kratos analytical (United Kingdom), Supra XPS, which had an automated water cooled 500mm quartz crystal monochromator X-ray source. Al Kα X-rays at 1486.7 eV are diffracted by an X-ray mirror consisting of quartz crystals

mounted on a toroid. The argon beam being from a multi-mode gas ion source offers the capability to generate both monatomic Ar^+ ions and Ar_n^+ cluster ions with n = 500 to 3000. Monatomic ions can be produced with beam energies from 500 eV to 8 keV. spot size: ≤ 500 µm. Data processed using ESCApe data-system. Atomic force microscopy (AFM) measurement was obtained using a HQ:NSC19/Al BS silicon tip back coated with aluminium (Mikromasch, France) connected to a Smart SPM1000 coupled to an XploRa PLUS V1.2 (using Omegascope AIST-NT v3.5 and LabSepc 6 respectively; Horiba, France) and a vibration isolation table, all carried out using AC mode. Samples were attached to magnetic disks using double sided tape.

4. Results and Discussion

Initially the bare graphene additive manufactured/3D-printed electrodes (Gr/AMEs) were produced from commercial conductive graphene/polylactic acid filament (see experimental section within the supporting information). An example of the produced Gr/AMEs can be observed within Figure 1(E). For full details of the Gr/AME production and their subsequent physicochemical and electrochemical characterization (including information on the specific chemicals and equipment utilized within this study) readers are directed to the electronic supporting information. Table 1 highlights a thorough literature review of the previous studies that have explored the electrocatalytic activity of nickel and nickel-iron (oxy)hydroxides electrocatalysts towards the OER. When combined with reduced graphene oxide (rGO), the performance of the hybrid material can be increased due to the synergistic effect between the catalytic activity of the nickel or nickel-iron (oxy)hydroxides and the fast electron transfer kinetics of rGO. In addition, oxygenated functional groups of rGO can improve the stability of the catalysts, due to the strong interactions with NiOOH or $Ni_xFe_{1-x}OOH$.[21] Thus, an electrochemical activation pre-treatment of the Gr/AMEs, consisting of two steps was performed. In the first step, a high anodic potential (+1.8 V) was applied for 15 minutes to create oxygen functionalities and exfoliated the graphene sheets, which are compacted in the polymeric matrix. In the second step, cyclic voltammetry was performed in cathodic direction to partially reduced the oxidized graphene structure and improve the electron transfer kinetics.[20b] After the pre-treatment, insulating PLA layer can be removed from the surface of the electrode, exposing the graphene sheets and, consequently, decreasing the charge transfer resistance (see Figure S1). The electrodeposition of Ni-Fe films on the pre-treated graphene AMEs was undertaken in cathodic conditions. Hydroxide ions are generated by the electrolytic decomposition of water (Equation 13), then, Ni^{2+} and Fe^{2+} ions react with produced OH^- to form bimetallic hydroxide at the interface of electrodes/solution (Equation 14).[15, 22]

$$2H_2O + e^- \rightarrow H_2 + 2OH^- \quad (13)$$

$$(1-x)\mathrm{Ni}^{2+} + x\mathrm{Fe}^{2+} + 2\mathrm{OH}^- \rightarrow \mathrm{Ni}_{1-x}\mathrm{Fe}_x(\mathrm{OH})_2 \qquad (14)$$

Figure 1 shows an illustration of the pre-treatment/electrodeposition and the electrochemical curves resulted from these processes, chronocoulometric, cyclic voltammogram and choronoamperometric curves. Electrocatalytic activities of the bare/unmodified and modified electrodes with respect to OER were investigated in 0.1 M KOH. Figure 2(A) shows the polarization curves of bare and modified Gr/AMEs with $Ni(OH)_2$ and $Ni_{1-x}Fe_x(OH)_2$, x = 5, 10, 20 and 40%. Note that the Gr/AME post pre-treatment and deposition were denoted as Gr/AME-Ni-$Fe_{x\%}$, where x is the percentage incorporation of Fe. The oxidation peak observed at + 1.49 V *vs.* RHE is assigned to electrochemical process between $Ni(OH)_2$ and NiOOH in alkaline media (Equation 15). The oxidation peak shift to more positive potentials with increasing the iron content, indicating changes in the electronic structure. The details of these changes and their precise effect on the catalysis mechanism remain unknown.[23]

$$\mathrm{Ni(OH)_2} + \mathrm{OH^-} \rightleftharpoons \mathrm{NiOOH} + \mathrm{H_2O} + \mathrm{e^-} \qquad (15)$$

Initially it was necessary to benchmark the OER activity of the bare/unmodified Gr/AME and a polycrystalline Ir electrode in 0.1 M KOH, the obtained CVs can be viewed in Figure 2(A). It is clear from this figure that the Gr/AME-Ni-$Fe_{x\%}$'s all had OER onset potentials of *ca*. +1.45 V (*vs*. RHE), which is comparable to that of polycrystalline Ir ((+ 1.43 V (*vs*. RHE)) and significantly less electropositive than the bare/unmodified Gr/AME. The significant increase in OER catalysis can be prescribed to the addition of the $Ni_{1-x}Fe_xOOH$ surface layer. The bare/unmodified Gr/AME achieved comparatively small current densities, even in high potentials, indicating negligible electrocatalytic activity toward the OER. The Ni and Ni-Fe films with 5, 10, 20 and 40 % Fe content show significant smaller overpotentials (*The overpotentials were determined at a geometric current density of 10 mA* cm^{-2}) of 771, 751, 519, 635 and 917 mV, respectively, which in the case of the Gr/AME-Ni-$Fe_{10\%}$ is close to the optimal of OER overpotential of Ir electrode (*ca.* 413 mV). These results indicate that the

Gr/AME-Ni-$Fe_{10\%}$ is an effective electrocatalyst towards OER. Tafel analysis (Figure 2(B) were performed on the Faradaic sections of the LSVs. The iridium electrode exhibited a small Tafel slope of 29 mV dec^{-1}, indicating a faster and efficient electrocatalytic process. The bare/unmodified Gr/AME exhibited a Tafel slope too large to be adequately interpreted by the Tafel analyses, it does however, show that the Gr/AME exhibits very poor OER activity. Upon modification of the Gr/AME with Ni-Fe (oxy)hydroxide layer there is a significant decrease in the Tafel Slope values obtained with the Gr/AME-Ni, Gr/AME-Ni-$Fe_{5\%}$, Gr/AME-Ni-$Fe_{10\%}$, Gr/AME-Ni-$Fe_{20\%}$ and Gr/AME-Ni-$Fe_{40\%}$'s exhibiting Tafel Slope values of 179, 167, 46, 70 and 60 mV dec^{-1}, respectively. The Tafel slopes deduced for the Gr/AME-Ni and 5% Ni-Fe (oxy)hydroxides suggest poor OER electrocatalytic activity as they are too large to be adequately explained *via* Tafel Analysis. The Gr/AME-Ni-$Fe_{10\%}$, Gr/AME-Ni-$Fe_{20\%}$ and Gr/AME-Ni-$Fe_{40\%}$'s displayed efficient electrocatalsis with the Gr/AME-Ni-$Fe_{10\%}$ displaying a near Ir Tafel value. The superior activity of these AMEs can be associated to the stabilization of the reaction intermediates (-OH, -O and -OOH).[24] It can be observed from Figure 2(C) that the electrocatalytic activity of Gr/AME-Ni-$Fe_{10\%}$ increased after 100 and 1000 cycles, probably due exposure of graphene-based material, since it has been reported that the protective layer of insulating PLA can be removed in hydroxide solution *via* saponification.[25]

In order to quantify the electrocatalytic activity on a per active site basis, the turnover frequencies (TOF) were calculated at an overpotential of 500 mV. Turnover frequencies were calculated *via* the Equation 16:

$$TOF = \frac{jA_eN_A}{4Fn} \qquad (16)$$

where j is the measured current density at an overpotential of 500 mV, A_e is the electrochemically active surface area of the working electrode (cm^2), N_A is the Avogadro constant, F is Faraday's constant, 4 is the number of electrons involved in the OER and n is the number of Ni sites present in the working electrode. In order to estimate the number of Ni sites involved in catalyzing the OER two

different techniques were used. In the first, we used a previously report values of 6.4 x 10^{14} for the Ni atom per cm^2, reported by Louie and Bell [14a], and the % Ni from the XPS data to calculate TOF_{max}. The second method involved determining the thickness of the films and the % Ni using a combination of XPS depth profiling and AFM with TERS to calculate TOF_{min}. Additionally, it was considered a monolayer thickness of *ca*. 8 Å for α-$Ni(OH)_2$ as reported by Trotochaud *et al*.[23] The values of TOF_{max} and TOF min are presented in Table S1. For the calculations, the compositions of the films were determined by X-ray photoelectron spectroscopy (XPS, Table S2). In addition, the thickness of the films (Table S3) were considered in order to estimate the TOF_{min}, assuming that all of Ni atoms are catalytic sites. In order to estimate the surface coverage of the electrodeposited Ni-Fe (oxy)hydroxides layer on the Gr/AME, XPS depth profiling was performed utilizing a Gr/AME-Ni-$Fe_{40\%}$ as a representative example. In order to penetrate the Ni-Fe (oxy)hydroxide layer and reveal the underlying graphene PLA substrate a 5 keV monoatomic Ar^+ beam was applied for 90 s intervals after which a XPS spectrum from 0 to 1200 eV was recorded (*N*=5 was utilized for increased peak resolution). Note the destructive process of applying the Ar^+ beam was expected to cause Ni and Fe contamination throughout the sampled area, therefore it was decided that upon the concentration of Fe (2p) and Ni (2p) reaching >5% it is likely that the graphene/PLA substrate had been reached. The initial spectrum recorded can be observed in Figure 3(A) where the concentrations of C(1s), Ni(2p), O(1s) and Fe(2p) were found to be 28.4, 11.1, 19.1 and 41.5%, respectively. It is of note that the percentage of Fe present within the surface coating matches the targeted 40% Fe concentration pre-determined in the fabrication technique. It can be seen in Figure 3(B) that there is a gradual decrease in the atomic % concentrations of Ni(2p), O(1s) and Fe(2p) and a corresponding increase in the concentration of C(1s) until etch number 52 when the atomic percentages of the C(1s), Ni(2p), O(1s) and Fe(2p) were recorded as 86.1, 2.5, 7.24 and 4.1%, respectively. Given that the atomic concentration of both Ni and Fe had dropped below 5% we concluded that underlying substrate (graphene PLA) had been reached, which would explain the high concentration of carbon.

XPS depth profiling allowed us to determine that the electrodeposited Ni-Fe (oxy)hydroxide layer on the Gr/AME-Ni-$Fe_{40\%}$ has been penetrated, however it is not possible to measure the depth of layer utilizing this technique. Therefore, AFM analysis was utilized to measure the depth between the non-etched surface of the Gr/AME-Ni-$Fe_{40\%}$ and the etch crater produced by the destructive Ar^+ beam. Figure 4(A) shows the recorded height profile taken from a cross section of the Ar+ beam crater upon Figure 4(B). Note the increased height at the etch site, this was found within all the sample sites and is likely due to a catering effect forcing material to accumulate at the etch sites periphery. Utilizing this technique at 5 separate sites it was possible to determine an average thickness of the Gr/AME-Ni-$Fe_{40\%}$ Ni-Fe (oxy)hydroxide layer (see Table S3). Tip Enhanced Raman Spectroscopy (TERS) was performed on the etch and non-etched areas of Gr/AME-Ni-$Fe_{40\%}$, as seen within the three dimensional model produced *via* AFM given in Figure 4(C). It is clear that the Raman spectrum taken from the non-etched area (location 2) had observable vibrational bands within the 300-550 cm^{-1} region,[26] which is characteristic of Ni and Fe based materials, that were not present in the etched area (location 1). This is further evidence that the Ni-Fe (oxy)hydroxide layer had been removed utilizing the Ar^+ beam. Further Raman spectra of the bare and modified electrodes are shown in Figure S2, the bands are assigned to network vibrational modes of graphene-based material.[27] Bands attributed to vibrational modes of the catalysts Ni or Ni-Fe (oxy)hydroxides were not observed, due to the low thickness of the films. The ratio between the D (~ 1350 cm^{-1}) and G (~ 1580 cm^{-1}) bands is an indicator the degree of disorder or structural defects of graphene network.[28]

Note that XRD and FTIR (See Figures Figures S3 and S4, respectively) was performed on the bare and modified AMEs. The diffractograms and the spectra show negligible change after the modification, probably due to low thickness of the films, ca. 40-90 nm (See Table S3). The x-ray and infrared beams usually penetrates the entire film making it impossible to follow structural variations as a function of film depth.[29]**.** As it can be seen in Table S4 and within the supporting information,

Gr/AME-Ni, Gr/AME-Ni-$Fe_{5\%}$, Gr/AME-Ni-$Fe_{10\%}$, Gr/AME-Ni-$Fe_{20\%}$ and Gr/AME-Ni-$Fe_{40\%}$ exhibited TOF_{min} of 0.21, 0.95, 2.11, 1.72 and 0.37, respectively.

To better understand the differences of the performances of the bare/unmodified and modified Gr/AMEs, their electrochemical properties were studied. It well known that the electrochemical properties of graphite and graphene-based electrodes are dependent on structural defects, presence of functional groups and exposure of edge and basal planes. Moreover, the main contribution on the electron transfer comes from the edge planes.[30] In this sense, the effect of the partial/complete coverage of these planes on the electrochemical properties of screen-printed graphene-like electrodes was investigated by Rowley-Neale *et al*.[31] The authors reported that MoO_2 films blocks the edge planes of graphene, reducing the electrochemical reactivity of the electrodes. The influence of the coverage of the 3D-printed graphene with Ni and Ni-Fe (oxy)hydroxides was studied by cyclic voltammetry, in the presence of the outer-sphere redox probe, $[Ru(NH)_6]^{3+}$, which is sensitive to electronic structure of the electrode materials, Figures S5 and S6. Additionally, the effect of the modification of the Gr/AMEs was investigated by electrochemical impedance spectroscopy (EIS, Figure S7), using the inner-sphere mediator $[Fe(CN)_6]^{4-/3-}$, which is sensitive to the surface chemistry of the electrodes. Thus, the charge transfer resistance (R_{CT}), the heterogeneous electron transfer rate constants using the inner (k°_{inner}) and outer-sphere (k°_{outer}) probes, and the number of edge planes (k°_{edge}) were determined and presented in Table S5. The bare Gr/AME presented the lowest value of R_{CT} due to the high conductivity of the graphene-based materials and the higher exposure of edge planes *ca.* 0.77%. After the modification with $Ni(OH)_2$, the electron transfer rates decreased, due to coverage of the edges planes of graphene on the surface ofIn the Gr/AME. Furthermore, the k°_{inner} decreased by approximately one order of magnitude, due to poor electrical conductivity of the $Ni(OH)_2$ film,[1] and the hindrance of charge transfer. The R_{CT} of the modified electrodes decreased upon electrodeposition of Fe. This result is consistent with previous reports, since the conductivity of nickel (oxy)hydroxide can increase by *ca.* 30-fold upon co-precipitation with Fe[23] thus, it can be expected that the electrode

with the highest content of iron should demonstrate the faster electron transfer kinetics. However, the bimetallic (oxy)hydroxide with 10% Fe concentration presented the lowest charge transfer resistance, probably due to the partial coverage of the 3D electrode, since the number of edge planes (k^{o}_{edge} = 0.59%) was the higher than the modified electrodes. In this sense, the best performance of the Gr/AME-Ni-$Fe_{10\%}$ towards OER can be associated to the optimal ratio of graphene edge planes/electrocatalytic sites.

According to Figure 5(A), the Gr/AME exhibited a relatively rough surface, which is consistent with previously reported additive manufactured electrodes.[20b] The electrochemical pre-treatment causes removal of PLA from the surface, exposing the electroactive sites of graphene. Similar wire-like morphology was recently reported by Browne *et al*.[32] who used a combination of chemical and electrochemical activations of PLA/graphene electrodes to improve their electrocatalytic activities towards hydrogen evolution reaction (HER). As it can be seen in Figure 5(B), the Gr/AME was completely covered by a film of $Ni(OH)_2$ film. The bimetallic films show vertically oriented flakes of Ni-Fe (oxy)hydroxides, which enlarge with an increased Fe content (see Figure 5(C-D) and Figure 5(F-G)). Additionally, Ni-Fe flakes were oriented as spheres on some regions of the surface of the Gr/AME-Ni-$Fe_{10\%}$ (see Figure 5(E)). The growth of micro-spheres with high surface area contributes to the improved performance of this electrode toward OER. The presence of titanium compounds was confirmed by EDS (Figure S8), which can contribute to the improvement of the activity after the 1000^{th} scan. Note that the XPS analysis (Table S2) and depth profiling did not detect the presence of titanium. However, cycling in 0.1 M KOH causes degradation of the polymeric matrix *via* saponification,[25] as it can be seen in Figure S9, exposing active graphene-based material and titanium catalytic sites. Therefore, as it can be seen in Table S4, the bare/unmodified electrode presented the lower value of I_D/I_G and the number of defects increased after modification. Our investigation implemented a technique for the electrodeposition of a Ni-Fe (oxy)hydroxide, with a tailorable Fe content, onto graphene incorporated additive manufactured/3D printed electrodes (Gr/AME-Ni-$Fe_{X\%}$) that would display efficient electrocatalysis towards the OER in alkaline medium. A stability test at a constant potential of 2.0 V *vs.* RHE for 10 hours. As it can be seen in Figure S10, the catalytic activity increases after the stability test, as a result of PLA removal *via* saponification and exposure of Ni-Fe catalyst electrodeposited in an inner layer of the electrodes.[25] Additionally, graphene-based material can be also exposed on the surface of the electrodes, facilitating the electron transfer. In order to investigate the ratio of Ni and Fe in the electrode submitted to 1000 cycles of stability in 0.1 M KOH

(Gr/AME-Ni-Fe10%; Post 1000 cycles), XPS measurements were performed (Table S2). As it can be seen Table S2, the ratio of Ni and Fe have similar values of 1.46 and 1.18 for the as-deposited film and the film submitted to 1000 cycles, respectively. XPS analysis was performed on the AMEs pre and post stability studies using the Gr/AME-Ni-$Fe_{10\%}$ (after 1000 cycles in 0.1 M KOH from 1.2 to 2.2 V *vs.* RHE), as it can be seen in the Figures S11 and S12. The Ni 2p spectra are shown in Figure S11, the main $2p_{3/2}$ peak was found in 885.7 eV, and a strong shake-up satellite was seen at approximately 862 – 863 eV binding energy. The spectra are typical of Ni^{2+}, but does not have the characteristic multiplet splitting or the correct binding energy for NiO. Instead, the spectrum is more characteristic of Ni^{2+} in $Ni(OH)_2$. The Fe 2p spectra (Figure S12) were very broad and not resolvable into separate chemically-shifted components. The Fe $2p_{3/2}$ peak energies are included in the table below, and were found at ~711 eV and relates iron oxide phases, including Fe_2O_3 and a possible FeOOH state.[14a] The XPS spectra for show negligible change after OER reflecting the stability of the AMEs produced.

5. Conclusion

In this paper we have explored the catalytic properties of polylactic acid/graphene additive manufactured electrodes (Gr/AMEs) electrodeposited with Ni-Fe (oxy)hydroxide. The Gr/AMEs catalytic performance to the OER in 0.1 M KOH was optimized by varying the concentration of Fe (5-40%) present within the Ni-Fe (oxy)hydroxide coating. A 10% incorporation of Fe resulted in the most beneficial OER catalysis, displaying an OER onset potential and overpotential of + 1.47 V (*vs*. RHE) and 519 mV, respectively, which is comparable to that of polycrystalline iridium (+ 1.43 V (*vs*. RHE) and *ca.* 413 mV). It is important to note that a bare/unmodified Gr/AME displays negligible OER activity.

This work is distinct from the literature for not only for being the first to electrodeposit Ni-Fe (oxy)hydroxide onto additive manufactured electrodes but also for describing a novel method of determining the mass/number of moles/thickness of the electrodeposited layer by a combination of spectroscopic and microscopic techniques.

This work describes the Gr/AMEs as a highly reproducible, cheap and tailorable electrolytic platforms that can be directly transferred to a plethora of applications within industrial and research-based activities. The fabricated Gr/AME-Ni-$Fe_{10\%}$ display remarkable OER activity and have the potential to increase feasibility of a hydrogen energy economy by increasing the overall efficiency of water splitting whilst additionally lowering its cost.

6. Acknowledgements

Funding from the Engineering and Physical Sciences Research Council (Reference: EP/P007767/1 and EP/N0011877/1), British Council Institutional Grant Link (No. 172726574) is acknowledged. The Manchester Fuel Cell Innovation Centre is funded by the European Regional Development Fund. This study was financed in part by the Coordenação de Aperfeiçoamento de Pessoal de Nível Superior - Brasil (CAPES) - Finance Code 001. The authors acknowledge the financial support by Fundo de Apoio ao Ensino, à Pesquisa e à Extensão - Universidade Estadual de Campinas, FAEPEX-UNICAMP (grant#2824/17) and Fundação de Amparo à Pesquisa do Estado de São Paulo, FAPESP (grant#2013/22127-2, grant#2017/23960-0). We thank Kratos Analytical, particularly Nikki Gerrard, for their help with the XPS data interpretation.

Key Words:

Energy Storage; Electrolysis; Additive Manufacturing; 3D Printing; Oxygen Evolution Reaction

Table 1. Currently literature reporting Ni-Fe (oxy)hydroxides-based electrocatalysts for the oxygen evolution reaction

Catalyst	Supporting Electrode	Electrolyte	OER overpotential mV at 10 mA cm^{-2}	Tafel slope mV dec^{-1}	Ref.
NiOOH	Au	0.1 M KOH	~ 480	55	[14a]
FeOOH	Au	0.1 M KOH	~530	54	[14a]
$Ni_{0.59}Fe_{0.41}OOH$	Au	0.1 M KOH	280	40	[14a]
Ni-Fe-LDH	GCE	1.0 M KOH	300	40	[16a]
Ni-Fe-LDH	GCE	1.0 M KOH	240	39	[14c]
Ni-Fe LDH nanoprisms	GCE	1.0 M KOH	280	49	[33]
Ni-Fe LDH nanoprisms	Ni-foam	1.0 M KOH	295	59	[33]
Ni-Fe nanosheets	Ni foam	0.1 M KOH	240	33	[15]
Ni-Fe-LDH platelets	Ni foam	0.1 M KOH	360	-	[9]
Ni-Fe-LDH	Ni foil	0.1 M KOH	410	58	[17]
Ni-Fe-LDH	Fe foil	0.1 M KOH	390	55	[17]
Ni-Fe-LDH	Ni-Fe alloy foil	0.1 M KOH	130	40	[17]
Ni-Fe-LDH/rGO	Ni foam	1.0 M KOH	195	40	[21]
Ni-Fe-LDH/NGF	GCE	0.1 M KOH	337	45	[34]
Ni-Fe-LDH/CNT	GCE	1.0 M KOH	300	31	[16b]
Gr/AME-Ni-$Fe_{10\%}$	AME	0.1 M KOH	519	46	This work

Key: LDH; layer double hydroxide, GCE; glassy carbon electrode, AME; additive manufactured (3D-printed) electrode

Figure 1. Schematic illustration for the pre-treatment and modification of the Gr/AME: compacted graphene sheets in the polymeric matrix (A), oxidation and exfoliation of the graphene sheets (B), electrodeposition of Ni or Ni-Fe (oxy)hydroxides (C). Digital picture and design of the Gr/AME (E). Electrochemical measurements showing the pre-treatment and electrodeposition: chronocoulometric curve (Q vs. t) of the as-printed AME under applied potential of +1.8 V in 0.1 M PB solution (F); cyclic voltammogram of the oxidized AME in 0.1 M phosphate buffer solution at 50 mV s^{-1} (G); chronoamperometric curve in Ni or Ni-Fe sulphate solution, under applied current density of –50 µA cm^{-2} (H).

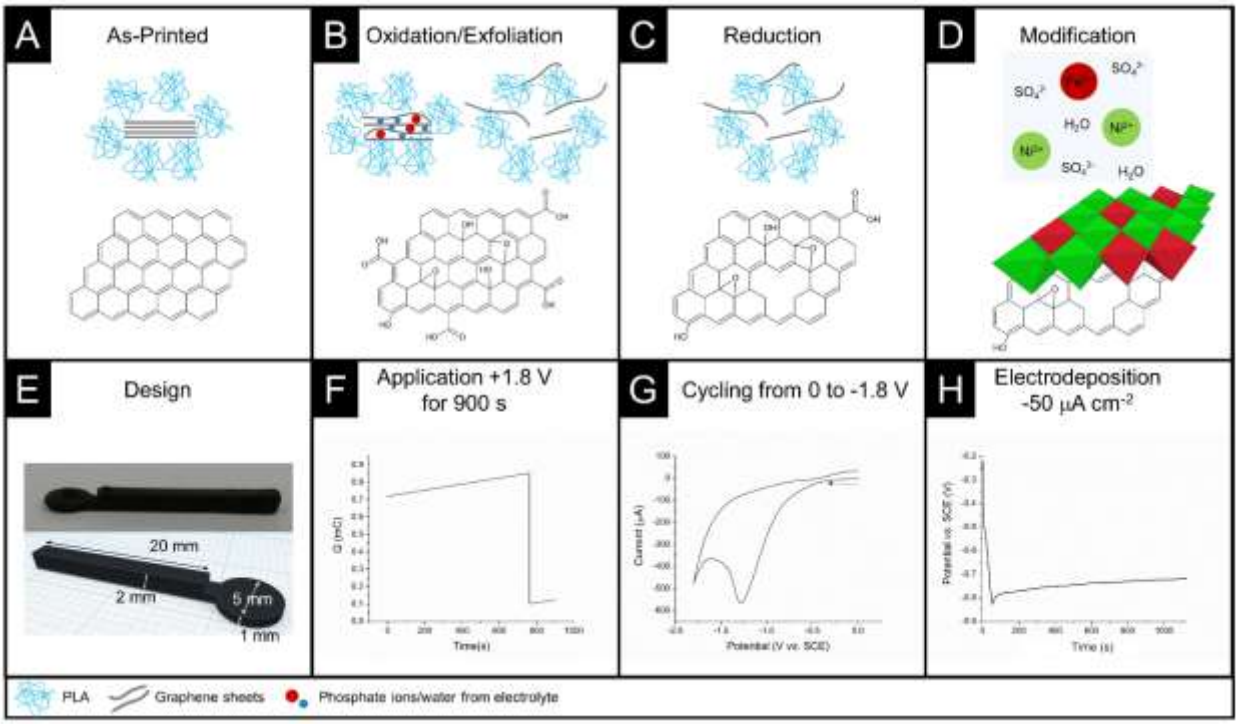

Figure 2. (A) Linear sweep voltammogram (LSVs) with 95% iR-compensation showing the OER activity of bare Gr/AME and the modified electrodes: Gr/AME-Ni, Gr/AME-Ni-$Fe_{5\%}$, Gr/AME-Ni-$Fe_{10\%}$, Gr/AME-Ni-$Fe_{20\%}$ and Gr/AME-Ni-$Fe_{40\%}$. Solution composition: 0.1 M KOH. Scan rate: 10 mV s^{-1}. (B) Tafel analysis; overpotential *vs.* log of current density for faradaic section of the LSV presented in (A). (C) Cyclic stability examination of the Gr/AME-Ni-$Fe_{10\%}$ *via* CV, repeated for 1000 cycles without iR-compensation. Solution composition: 0.1 M KOH. Scan rate: 100 mV s^{-1}.

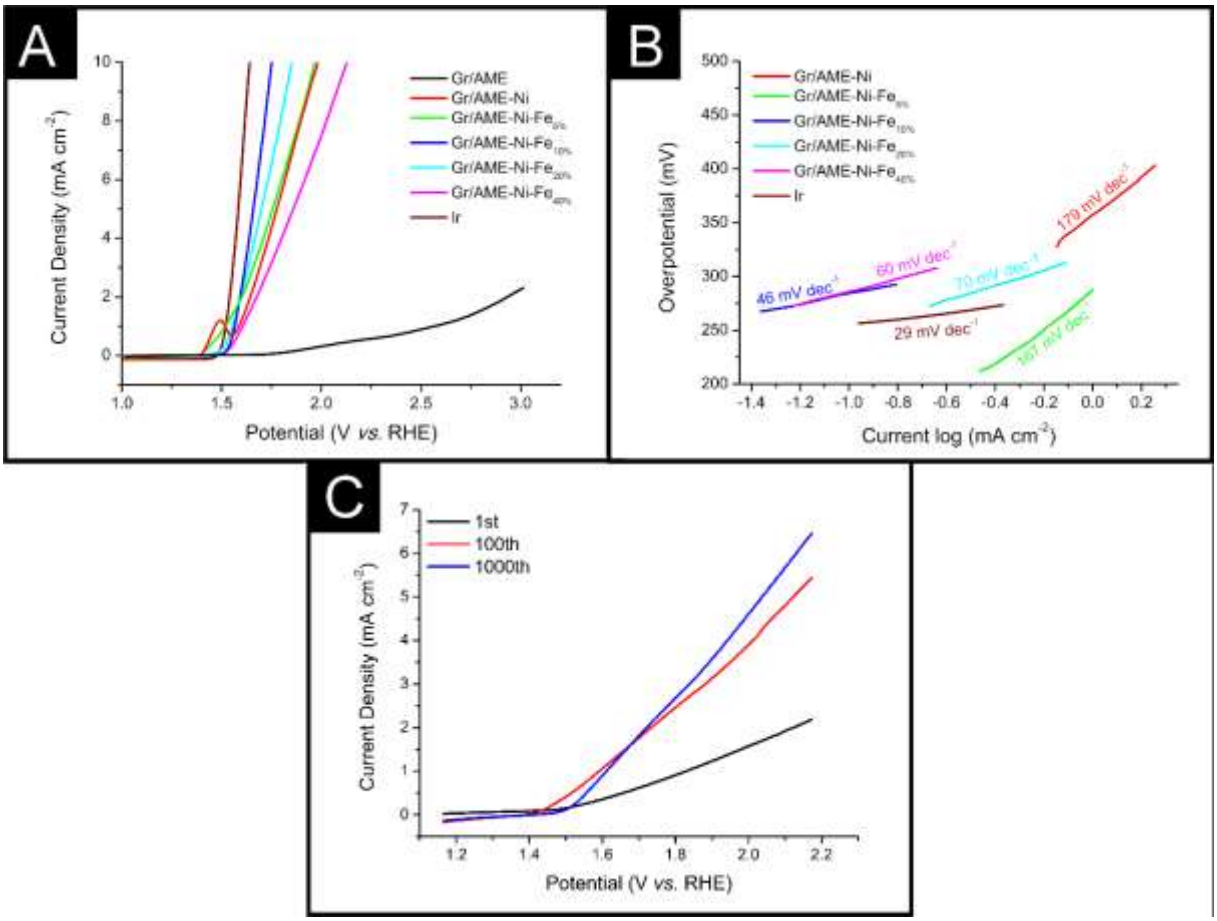

Figure 3. (A) XPS depth profiling of a Gr/AME-Ni-$Fe_{40\%}$. The depth profiling consisted of a 5 keV monoatomic Ar+ beam applied for 52 intervals of 90 second etches with a XPS spectrum (N=5 to ensure peak resolution) initiated 15 seconds post each etch. The elemental percentage composition of C, Ni, O and Fe after each etch is shown in (B).

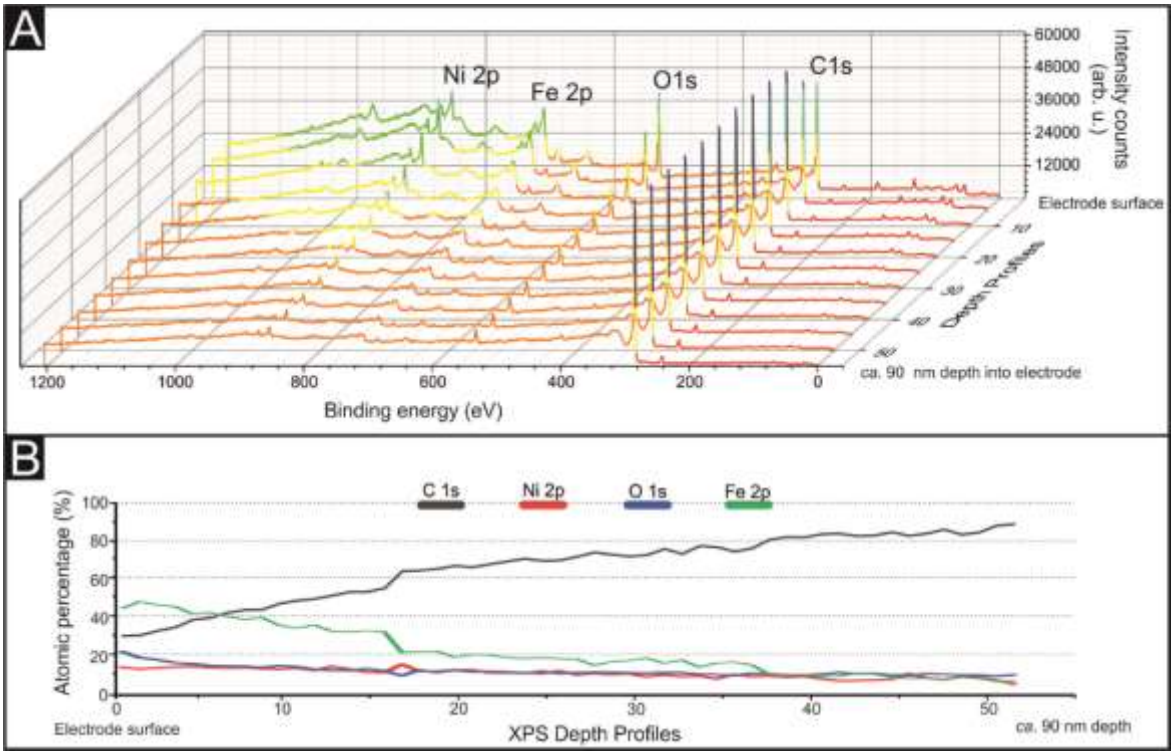

Figure 4. Atomic force microscope (AFM) images of the step produced in the Gr/AME-Ni-$Fe_{40\%}$ by the Argon beam (5 keV monoatomic Ar+ beam applied for 52 intervals of 90 second etches) utilized within Figure 3 depth profiling (A) with the AMEs cross section being given in (B). (C) 3D AFM map of the Gr/AME-Ni-$Fe_{40\%}$ etch crater with Tip Enhanced Raman Spectroscopy (TERS) of the Gr/AME-Ni-$Fe_{40\%}$ etched (1) and non-etched surface (2) areas.

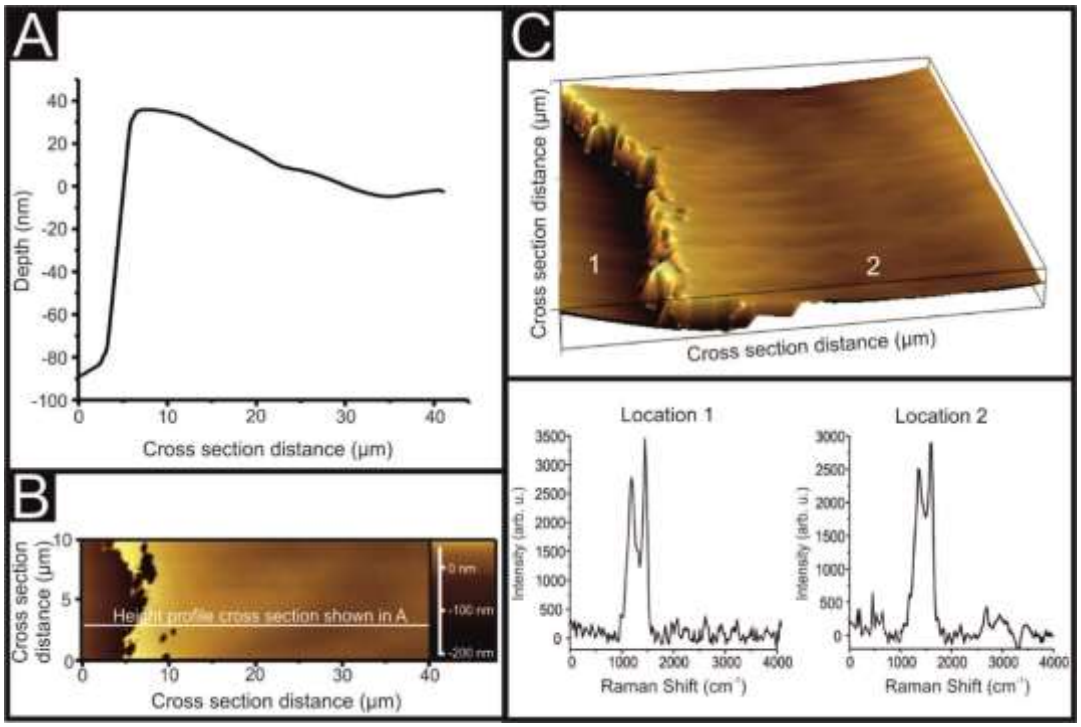

Figure 5. Field emission scanning electron microscopy (FEG-SEM) micrographs of (A) bare Gr/AME and the modified electrodes: (B) Gr/AME-Ni, (C) Gr/AME-Ni-$Fe_{5\%}$, (D, E) Gr/AME-Ni-$Fe_{10\%}$, (F) Gr/AME-Ni-$Fe_{20\%}$ and (G) Gr/AME-Ni-$Fe_{40\%}$. Scale bars correspond to 1 µm.

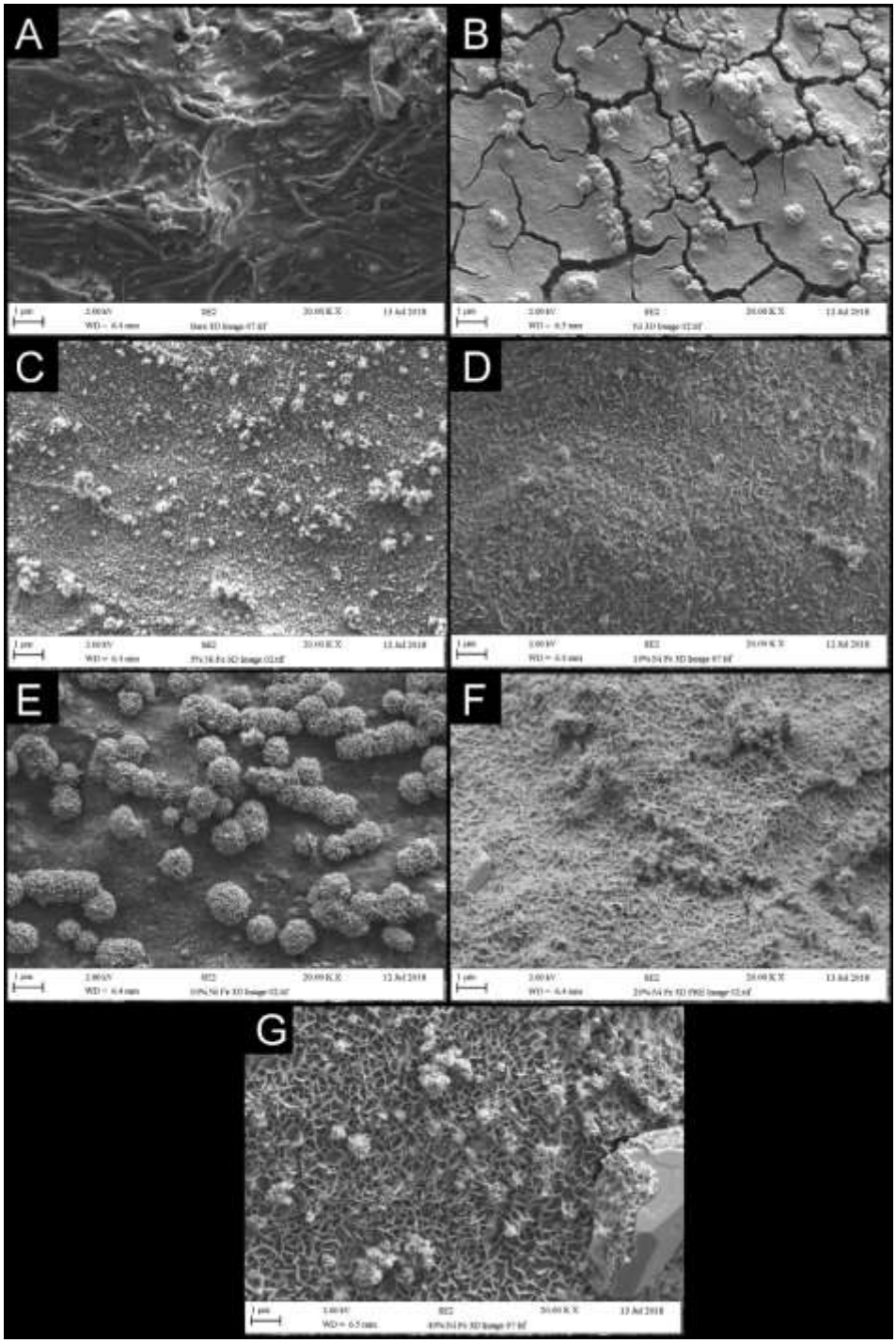

7. References

[1] https://www.iea.org/publications/wei2017/, *Vol. 2019*, IEA, Paris, **2017**.

[2] aS. J. Rowley-Neale, M. Ratova, L. T. N. Fugita, G. C. Smith, A. Gaffar, J. Kulczyk-Malecka, P. J. Kelly, C. E. Banks, *ACS Omega* **2018**, *3*, 7235-7242; bA. Ahmed, A. Q. Al-Amin, A. F. Ambrose, R. Saidur, *Int. J. Hydrogen Energy* **2016**, *41*, 1369-1380.

[3] M. S. Burke, L. J. Enman, A. S. Batchellor, S. Zou, S. W. Boettcher, *Chem. Mater.* **2015**, *27*, 7549-7558.

[4] N.-T. Suen, S.-F. Hung, Q. Quan, N. Zhang, Y.-J. Xu, H. M. Chen, *Chem. Soc. Rev.* **2017**, *46*, 337-365.

[5] R. L. Doyle, M. E. G. Lyons, in *Photoelectrochemical Solar Fuel Production: From Basic Principles to Advanced Devices* (Eds.: S. Giménez, J. Bisquert), Springer International Publishing, Cham, **2016**, pp. 41-104.

[6] X. Li, X. Hao, A. Abudula, G. Guan, *J. Mater. Chem. A* **2016**, *4*, 11973-12000.

[7] aO. Kasian, J.-P. Grote, S. Geiger, S. Cherevko, K. J. J. Mayrhofer, *Angew. Chem. Int. Ed.* **2018**, *57*, 2488-2491; bM. Wohlfahrt-Mehrens, J. Heitbaum, *J. Electroanal. Chem. Interfacial Electrochem.* **1987**, *237*, 251-260.

[8] B. M. Pires, P. L. d. Santos, V. Katic, S. Strohauer, R. Landers, A. L. B. Formiga, J. A. Bonacin, *Dalton Trans.* **2019**, *48*, 4811-4822.

[9] S. Jaśkaniec, C. Hobbs, A. Seral-Ascaso, J. Coelho, M. P. Browne, D. Tyndall, T. Sasaki, V. Nicolosi, *Sci. Rep.* **2018**, *8*, 4179.

[10] aJ. Ahmed, T. Ahamad, S. M. AlShehri, *ChemElectroChem* **2017**, *4*, 1222-1226; bJ. Ahmed, B. Kumar, A. M. Mugweru, P. Trinh, K. V. Ramanujachary, S. E. Lofland, Govind, A. K. Ganguli, *J. Phys. Chem. C* **2010**, *114*, 18779-18784.

[11] A. Ambrosi, M. Pumera, *Chem. Soc. Rev.* **2016**, *45*, 2740-2755.

[12] J. O. Bockris, *J. Electrochem. Soc.* **1984**, 290–302.

[13] V. Fidelsky, M. C. Toroker, *Phys. Chem. Chem. Phys.* **2017**, *19*, 7491-7497.

[14] aM. W. Louie, A. T. Bell, *J. Am. Chem. Soc.* **2013**, *135*, 12329-12337; bD. Friebel, M. W. Louie, M. Bajdich, K. E. Sanwald, Y. Cai, A. M. Wise, M.-J. Cheng, D. Sokaras, T.-C. Weng, R. Alonso-Mori, R. C. Davis, J. R. Bargar, J. K. Nørskov, A. Nilsson, A. T. Bell, *J. Am. Chem. Soc.* **2015**, *137*, 1305-1313; cM. Görlin, P. Chernev, J. F. d. Araújo, T. Reier, S. Dresp, B. Paul, R. Krähnert, H. Dau, P. Strasser, *J. Am. Chem. Soc.* **2016**, *138*, 5603-5614; dJ. Ahmed, S. Sharma, K. V. Ramanujachary, S. E. Lofland, A. K. Ganguli, *J. Colloid Interface Sci.* **2009**, *336*, 814-819.

[15] X. Lu, C. Zhao, *Nat. Commun.* **2015**, *6*, 6616.

[16] aF. Song, X. Hu, *Nat. Commun.* **2014**, *5*, 4477; bM. Gong, Y. Li, H. Wang, Y. Liang, J. Z. Wu, J. Zhou, J. Wang, T. Regier, F. Wei, H. Dai, *J. Am. Chem. Soc.* **2013**, *135*, 8452-8455.

[17] Q. Xiang, F. Li, W. Chen, Y. Ma, Y. Wu, X. Gu, Y. Qin, P. Tao, C. Song, W. Shang, H. Zhu, T. Deng, J. Wu, *ACS Energy Lett.* **2018**, *3*, 2357-2365.

[18] aC. Y. Foo, H. N. Lim, M. A. Mahdi, M. H. Wahid, N. M. Huang, *Sci. Rep.* **2018**, *8*, 7399; bC. W. Foster, M. P. Down, Y. Zhang, X. Ji, S. J. Rowley-Neale, G. C. Smith, P. J. Kelly, C. E. Banks, *Sci. Rep.* **2017**, *7*, 42233.

[19] M. P. Down, E. Martínez-Periñán, C. W. Foster, E. Lorenzo, G. C. Smith, C. E. Banks, *Adv. Energy Mater.* **2019**, *9*, 1803019.

[20] aR. M. Cardoso, D. M. H. Mendonça, W. P. Silva, M. N. T. Silva, E. Nossol, R. A. B. d. Silva, E. M. Richter, R. A. A. Muñoz, *Anal. Chim. Acta* **2018**, *1033*, 49-57; bP. L. d. Santos, V. Katic, H. C. Loureiro, M. F. d. Santos, D. P. d. Santos, A. L. B. Formiga, J. A. Bonacin, *Sens. Actuators, B* **2019**, *281*, 837-848.

[21] X. Long, J. Li, S. Xiao, K. Yan, Z. Wang, H. Chen, S. Yang, *Angew. Chem. Int. Ed.* **2014**, *53*, 7584-7588.

[22] M. Wohlfahrt-Mehrens, R. Oesten, P. Wilde, R. A. Huggins, *Solid State Ionics* **1996**, *86-88*, 841-847.
[23] L. Trotochaud, S. L. Young, J. K. Ranney, S. W. Boettcher, *J. Am. Chem. Soc.* **2014**, *136*, 6744-6753.
[24] J. R. Swierk, S. Klaus, L. Trotochaud, A. T. Bell, T. D. Tilley, *J. Phys. Chem. C* **2015**, *119*, 19022-19029.
[25] D. M. Wirth, M. J. Sheaff, J. V. Waldman, M. P. Symcox, H. D. Whitehead, J. D. Sharp, J. R. Doerfler, A. A. Lamar, G. LeBlanc, *Anal. Chem.* **2019**, *91*, 5553-5557.
[26] M. Gong, H. Dai, *Nano Res.* **2015**, *8*, 23-39.
[27] A. C. Ferrari, *Solid State Commun.* **2007**, *143*, 47-57.
[28] L. M. Malard, M. A. Pimenta, G. Dresselhaus, M. S. Dresselhaus, *Phys. Rep.* **2009**, *473*, 51-87.
[29] aG. Lim, W. Parrish, C. Ortiz, M. Bellotto, M. Hart, *J. Mater. Res.* **1987**, *2*, 471-477; bA. K. L. Andrew, S. G. Kazarian, *Chem. Soc. Rev.* **2016**, *45*, 1850-1864.
[30] aD. K. Kampouris, C. E. Banks, *Chem. Commun.* **2010**, *46*, 8986-8988; bD. A. C. Brownson, L. J. Munro, D. K. Kampouris, C. E. Banks, *RSC Adv.* **2011**, *1*, 978-988; cD. A. C. Brownson, D. K. Kampouris, C. E. Banks., *Chem. Soc. Rev.* **2012**, *41*, 6944-6976.
[31] S. J. Rowley-Neale, D. A. C. Brownson, C. E. Banks, *Nanoscale* **2016**, *8*, 15241-15251.
[32] C.-C. Yang, *Int. J. Hydrogen Energy* **2002**, *27*, 1071-1081.
[33] L. Yu, J. F. Yang, B. Y. Guan, Y. Lu, X. W. Lou, *Angew. Chem. Int. Ed.* **2018**, *57*, 172-176.
[34] C. Tang, H.-S. Wang, H.-F. Wang, Q. Zhang, G.-L. Tian, J.-Q. Nie, F. Wei, *Adv. Mater.* **2015**, *27*, 4516-4522.